European Journal of
Mineralogy
Open Access

Kahlenbergite $KAl_{11}O_{17}$, a new β-alumina mineral and Fe-rich hibonite from the Hatrurim Basin, the Negev desert, Israel

Biljana Krüger[1], **Evgeny V. Galuskin**[2], **Irina O. Galuskina**[1], **Hannes Krüger**[1], **and Yevgeny Vapnik**[3]

[1]Institute of Mineralogy and Petrography, University of Innsbruck, Innrain 52, 6020 Innsbruck, Austria
[2]Faculty of Natural Sciences, Institute of Earth Sciences, University of Silesia, Będzińska 60, 41-200 Sosnowiec, Poland
[3]Department of Geological and Environmental Sciences, Ben-Gurion University of the Negev, P.O. Box 653, Beer-Sheva 84105, Israel

Correspondence: Biljana Krüger (biljana.krueger@uibk.ac.at)

Abstract. Kahlenbergite, ideally $KAl_{11}O_{17}$, and Fe-rich hibonite, $CaAl_{10}Fe_2O_{19}$, are high-temperature minerals found in "olive" subunits of pyrometamorphic rocks, in the Hatrurim Basin, the Negev desert, Israel. The crystal structures of both minerals are refined using synchrotron radiation single-crystal diffraction data. The structure of kahlenbergite ($P6_3/mmc$; $a = 5.6486(1)$ Å; $b = 22.8970(3)$ Å; $Z = 2$) exhibits triple spinel blocks and so-called R blocks. The spinel blocks show mixed layers with AlO_6 octahedra and $(Al_{0.56}Fe_{0.44})O_4$ tetrahedra and kagome layers with $(Al_{0.92}Fe_{0.08})O_6$ octahedra. One-dimensional diffuse scattering observed parallel to c^* implies stacking faults in the structure. Also, in one of the investigated kahlenbergite crystals additional reflections can be identified, which obviously belong to a second phase with a smaller lattice parameter c: Fe^{3+}-rich hibonite. The structure of hibonite contains the same spinel blocks as kahlenbergite. The R blocks in hibonite contain Ca atoms, AlO_5 bipyramids, and AlO_6 octahedra, whereas the R blocks in kahlenbergite contain potassium atoms and AlO_4 tetrahedra.

1   Introduction

The β-alumina compounds with mono-valent cations, like sodium and potassium, are known as fast ion conductors. Furthermore, they often exhibit nonstoichiometric composition and disordered structures (Collin et al., 1986a, b; Kim et al., 2018). To date, only two minerals with structures of the β-alumina type are known: kahlenbergite and diaoyudaoite.

The new mineral kahlenbergite (IMA2018-158) with the endmember formula $KAl_{11}O_{17}$ is found in small hematite segregations enriched by hibonite within wollastonite–gehlenite hornfels, north-east of Mt Parsa, the Hatrurim Basin, the Negev desert, Israel. It is a high-temperature mineral that occurs together with hibonite, corundum, hematite, dorrite and other anhydrous minerals. Kahlenbergite and associated minerals crystallize at temperatures of not less than 1000 °C under strongly oxidizing conditions.

A second occurrence of kahlenbergite with the composition $K_{1.05}(Al_{10.84}Cr^{3+}_{0.11}Cr^{2+}_{0.04}Mg_{0.01})_{\Sigma 11}O_{17}$ is reported in corundum separates from bulk rock probes of the Upper Cretaceous pyroclastics at Mount Carmel, north Israel (Griffin et al., 2020a, b), along with Cr-rich corundum and diaoyudaoite, a sodium β-alumina type phase. There is opinion that corundum with unusual inclusions from Mount Carmel has anthropogenic genesis (Litasov et al., 2019; Ballhaus et al., 2021).
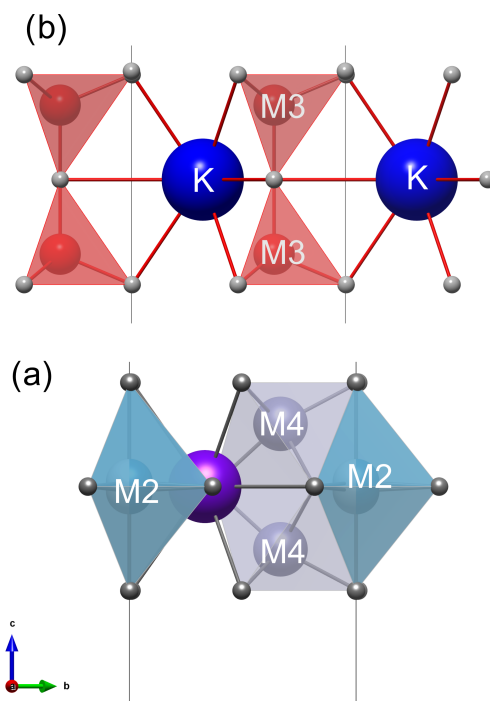
The mineral diaoyudaoite (IMA1985-05), sodium β-alumina $NaAl_{11}O_{17}$, was first found in the heavy metal fraction in sea-floor muds at about a 1500 m water depth, near the Diaoyu/Senkaku Islands (Shen et al., 1986; Zhu et al., 1992). Further investigation by Ying et al. (1998) indicated that this phase may originate from metallurgical industry waste that has been re-transported underwater near the southern end of the Okinawa Trough. Diaoyudaoite found in the Newark Bay
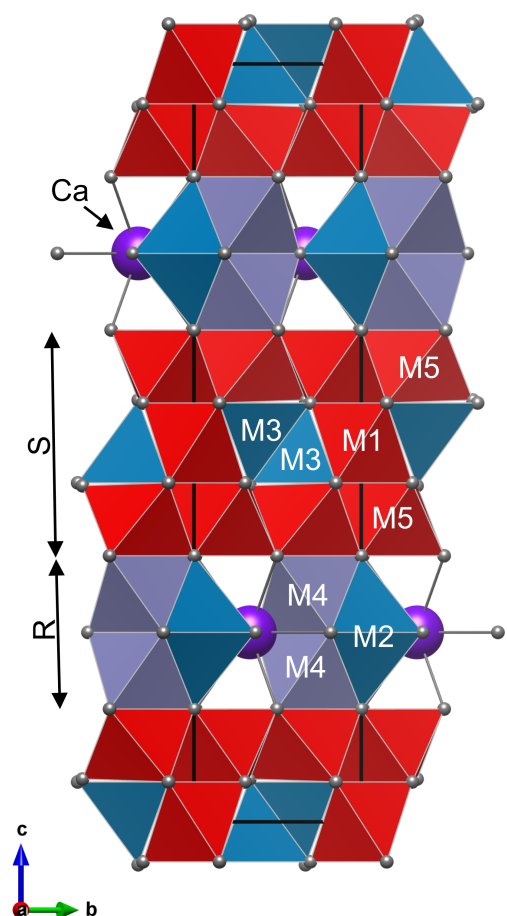
Figure 1. Structure of hibonite $CaAl_{10}Fe_2O_{19}$ with cation sites M1–M5: unit cell is made of two spinel blocks (S) and two conducting blocks (R). Colours of polyhedra show occupancy of M sites: pure Al in red, (Al, Fe) polyhedra in teal, and (Al, Fe, Ti) octahedra in lilac.

Figure 2. Conducting R blocks in **(a)** magnetoplumbite-type structure with five coordinated M2 cations and **(b)** kahlenbergite with four coordinated M3 cations.

channel, New Jersey, USA, was also dredged from a locality close to a former chromium smelter (https://www.mindat.org/loc-14038.html, last access: 28 June 2021). An anthropogenic analogue of diaoyudaoite is known as a byproduct of Cr smelting (Sorokina and Iospa, 2012) and is a common impurity in synthetic corundum (Al-Shantir et al., 2020; Pawlowski and Blanchart, 2018).

Until recently, diaoyudaoite has been attributed to the magnetoplumbite group, which, however, has not been defined and/or approved by the IMA CNMNC. In 2020, Holtstam and Hålenius (2020) published a new CNMNC-approved nomenclature and classification scheme for the magnetoplumbite group with the general formula $AB_{12}O_{19}$, where A is a large cation (A^{2+} or A^{1+}) and B usually represents more highly charged cations of intermediate size. The group discerns the following subgroups based on the dominant A-type cation: magnetoplumbite ($A = Pb$), hawthorneite ($A = Ba$), and the hibonite ($A = Ca$) subgroup. Chihuahuaite $FeAl_{12}O_{19}$, previously known as hibonite-(Fe),

with $A = (Fe^{2+}, Mg)$ and yimengite $K(Cr,Ti,Fe,Mg)_{12}O_{19}$ (IMA1982-046) with $A = K$ remain ungrouped members of the magnetoplumbite group. The known β-alumina-type minerals diaoyudaoite, $NaAl_{11}O_{17}$ (Shen et al., 1986), and kahlenbergite, $KAl_{11}O_{17}$ (Krüger et al., 2019), cannot be members of the magnetoplumbite group because their structures, although related, are not isotypic to magnetoplumbite (Holtstam and Hålenius, 2020).

The structure of magnetoplumbite group minerals, as well as of kahlenbergite and diaoyudaoite, can be explained by stacking of spinel (S) and conducting (R) blocks along the hexagonal c axis (Fig. 1). The S block is a sequence of two cubic closest-packed oxygen layers with smaller cations distributed at octahedrally and tetrahedrally coordinated sites. The R block is a sequence of three hexagonal closest-packed oxygen layers (Kohn and Eckart, 1964; Iyi et al., 1989). In the central layer of the R block, one of four oxygen atoms is replaced by an A cation. In the magnetoplumbite structure, one of the smaller B cations (M2 site) is five-coordinated, whereas in the structure of kahlenbergite and diaoyudaoite the smaller cations (M3 site) are tetrahedrally coordinated (Fig. 2).

The name kahlenbergite is chosen in honour of Volker Kahlenberg (b. 1964), professor of applied mineralogy and crystallography at the University of Innsbruck, Austria, since 2003. He has served as president and vice president of the Austrian Mineralogical Society (ÖMG). Since 2017 he has

Figure 3. (a) Wollastonite–gehlenite hornfels (arrow) is distinguished by a dark colour against the background of light-coloured rocks of the Hatrurim Complex altered during low-temperature processes. **(b)** Dense and hard hornfels contains small segregations of hematite (arrows), in some of which has been found kahlenbergite in light-brown fragments of the rock.

been a member of the IUCr Commission on Inorganic and Mineral Structures.

Type material was deposited in the mineralogical collection of the Fersman Mineralogical Museum, Leninskiy Prospekt 18, k2, 115162 Moscow, Russia, catalogue number 96587.

2 Occurrence and paragenesis

Circa 300 m north-east of the top of Mt Parsa (Har Parsa) (31°12.18′ N, 36°15.31′ E) within the biggest field of pyrometamorphic rocks in the Negev desert, known as the Hatrurim Basin, kahlenbergite occurs in small hematite segregations within wollastonite–gehlenite hornfels (Fig. 3a, b). This is the largest occurrence of the pyrometamorphic rocks in the Dead Sea rift area in the territory of Israel (Geller et al., 2012; Novikov et al., 2013) and a part of the Hatrurim Complex (Mottled Zone) (Bentor, 1960; Gross, 1977). Hematite segregations (enclaves) (Fig. 4a) with kahlenbergite occur in wollastonite–gehlenite hornfels, which are similar to rock belonging to the so-termed "olive unit" (Fig. 3b; Bentor and Vroman, 1960).

Occasionally, hornfels shows a vesicular texture, which is an indicator for partial melting. The main minerals of hornfels are wollastonite, gehlenite, esseneite-diopside, andradite, and anorthite. Sometimes, minerals of the levantite–latiumite series (Galuskin et al., 2019) and celsian appear in a substantial amount. Minerals of the spinel–magnesioferrite series, hematite, baryte, and Si-bearing apatite are accessory minerals. Vesicular spaces are filled with zeolites, Ca hydrosilicates, and occasionally with calcite and ettringite.

Hematite segregations exhibit different minerals including various ferrites and aluminates. Hematite enclaves with kahlenbergite are enriched in hibonite (Fig. 4c). Moreover, spinel, corundum, and pseudobrookite are present in association with kahlenbergite (Fig. 4c, d). Dorrite was detected at the boundary of the hematite segregation with hornfels. The Fe^{3+} analogue of hibonite – new mineral gorerite
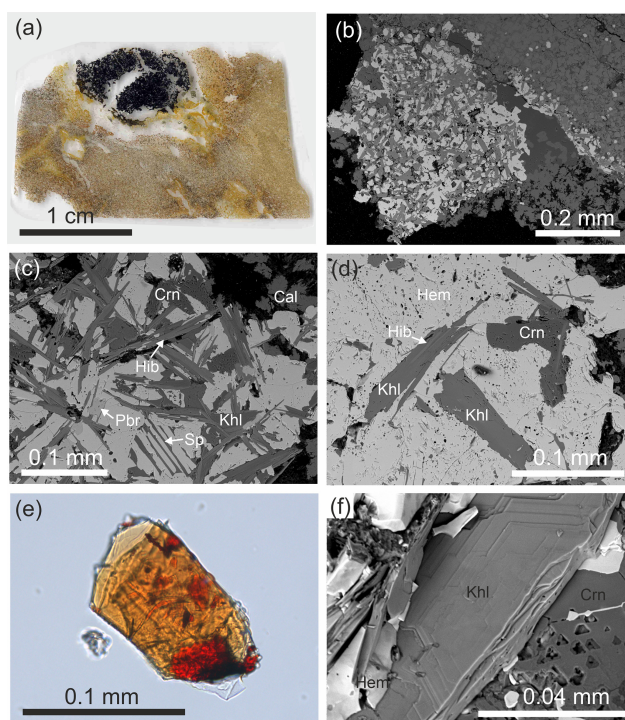
Figure 4. (a) Hematite segregation in wollastonite–gehlenite hornfels with grey-green esseneite crystals around it; **(b)** hematite enclave with a significant amount of hibonite, spinel, corundum, and dorrite; **(c)** hibonite overgrows and replaces kahlenbergite; **(d)** rare, relatively large kahlenbergite crystals in hematite; **(e)** kahlenbergite crystal flattened on (001) with epitaxial inclusions of hibonite (orange) and spinel inclusion (red); optical photo in immersion with $n = 1.63$; **(f)** fragment of flattened kahlenbergite crystal with hexagonal elements of microrelief. Mineral symbols are hibonite (Hib), spinel (Sp), corundum (Crn), calcite (Cal), kahlenbergite (Khl), hematite (Hem), and pseudobrookite (Pbr).

Table 1. Chemical composition of kahlenbergite from Mt Parsa (in wt %).

| Constituent	Mean	Range	SD (σ)
Na$_2$O	0.02	0–0.06	0.02
K$_2$O	6.29	5.77–6.65	0.22
MgO	1.43	0.61–2.22	0.44
CaO	0.25	0.01–0.82	0.24
MnO	0.05	0–0.09	0.02
BaO	0.17	0.09–0.25	0.04
Al$_2$O$_3$	74.05	70.26–76.08	1.62
Cr$_2$O$_3$	0.19	0.12–0.30	0.04
Fe$_2$O$_3$	16.70	14.78–19.09	1.17
SiO$_2$	0.15	0.02–0.52	0.14
Total	99.30		

CaAlFe$_{12}$O$_{19}$ (Galuskin et al., 2019) – is observed in spinel exsolutions.

3 Appearance and physical properties of kahlenbergite

Kahlenbergite forms platy crystals flattened on (001). They are up to 0.2 mm in diameter, and the thickness usually does not exceed 0.02 mm (Fig. 4e, f). The colour is light brown, yellow-brown, or light orange. Small grains and thin sections of kahlenbergite are optically transparent. The lustre is vitreous, and the streak is light brown. Cleavage parallel to {001} is good. Fracture is conchoidal set at an angle to (001) and stepped on (001). Parting is not observed, and tenacity is brittle. Fluorescence is not observed. The microhardness VHN$_{50}$ = 1199(76) kg mm^{-2} (mean-of-18 analyses correspond to 6–7 on the Mohs scale. Density is not measured because of the small size of the crystals and numerous inclusions. Based on the empirical formula and the unit cell volume, obtained from single-crystal data, the density of kahlenbergite is calculated to be 3.40 g cm^{-3}. Kahlenbergite is epitaxially replaced and overgrown by hibonite (Fig. 4c–e). Most of the kahlenbergite crystals contain hibonite inclusions (Fig. 4e). Optically, kahlenbergite is uniaxially negative, with $\omega = 1.795(3)$ and $\varepsilon = 1.785(3)$ for $\lambda = 589$ nm, and does not exhibit pleochroism. All investigations were performed on kahlenbergite grains from the small (~ 1 cm) holotype specimen. The appearance and physical properties of hibonite in pyrometamorphic rocks of the Hatrurim Basin in Israel are reported by Sharygin (2019).

4 Experimental methods

Quantitative chemical analyses of kahlenbergite and hibonite were performed using a Cameca SX100 electron microprobe (Institute of Geochemistry, Mineralogy and Petrology, University of Warsaw) operated in wavelength dispersive mode
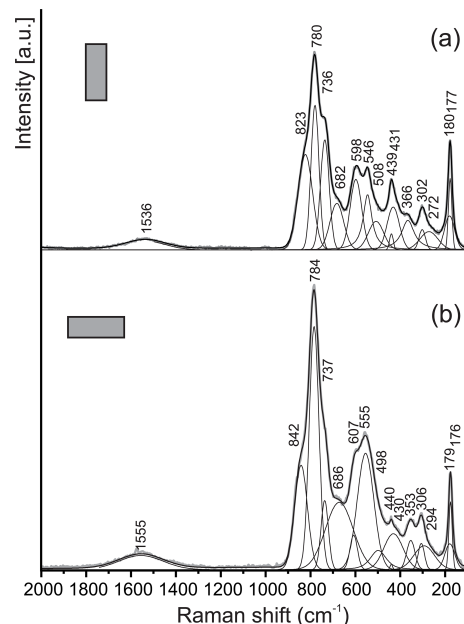
Figure 5. Raman spectra of kahlenbergite for two orientations of crystals. Laser beam is polarized horizontally.

at 15 kV and 20 nA with a 2 µm beam diameter. The following standards were used for the analysis of the given elements ($K\alpha$ lines): albite (Na), orthoclase (K, Na), dolomite (Mg), wollastonite (Ca, Si), rhodonite (Mn), rutile (Ti), V metal (V), celestine (Sr), Cr$_2$O$_3$ (Cr), hematite (Fe), and baryte (Ba $L\beta$). Results are given in Tables 1 and 2.

Raman spectra of kahlenbergite and hibonite (Figs. 5 and 6) were recorded on polished sections. A WITec alpha300 R confocal Raman microscope (Institute of Earth Sciences, University of Silesia, Poland) equipped with an air-cooled solid laser (532 nm) and a CCD camera operating at -61 °C was used. The laser radiation was coupled to a microscope through a single-mode optical fibre with a diameter of 3.5 µm. A Zeiss LD EC Epiplan-Neofluar DIC 100$\times$/0.75 NA air objective was used. Raman-scattered light was focused on a broadband single-mode fibre with an effective pinhole size of about 30 µm and monochromator with a 600 mm^{-1} grating. The power of the laser at the sample position was ~ 30 mW. Integration times of 3 s with accumulations of 15 scans and a resolution of 3 cm^{-1} were chosen. The monochromator was calibrated using the Raman-scattering line of a silicon plate (520.7 cm^{-1}). Fitting of spectra was performed with the help of the GRAMS/AI (Thermo Fisher Scientific) program using the mixed Lorentz and Gauss functions.

Single-crystal diffraction experiments in ambient conditions were performed at the X06DA beamline at the Swiss Light Source (Paul Scherrer Institute, Villigen, Switzerland). The beamline is equipped with a one-circle Aerotech goniometer and a PILATUS 2M-F detector. Data collection

Table 2. Two type of hibonites from Mt Parsa, the Negev desert, Israel.

Constituent	Low-Ti hibonite[a]			High-Ti hibonite[b]		
	Mean 10	SD	Range	Mean 6	SD	Range
TiO_2	3.07	1.23	0.55–4.84	8.76	0.24	8.53–9.15
SiO_2	0.04	0.03	0.01–0.10	0.10	0.06	0.05–0.20
Fe_2O_3	20.17	2.21	15.84–24.25	20.27	1.22	18.19–21.43
Cr_2O_3	1.03	0.16	0.79–1.41	0.11	0.03	0.08–0.16
V_2O_3	0.35	0.08	0.22–0.48	0.06	0.04	0–0.09
Al_2O_3	66.36	2.87	61.75–70.99	58.21	0.97	57.34–59.69
BaO	n.d.			0.08	0.08	0–0.20
SrO	n.d.			0.07	0.07	0–0.16
FeO^c				3.14	1.00	1.53–4.01
MnO	n.d.			0.10	0.06	0–0.14
CaO	7.92	0.08	7.81–8.06	7.44	0.51	6.75–8.17
MgO	1.42	0.43	0.68–2.00	2.12	0.54	1.47–2.98
K_2O	n.d.			0.16	0.16	0–0.38
Na_2O	n.d.			0.11	0.01	0.10–0.12
Total	100.36			100.75		
Calculated on 19O and charge balance						
Ca	1.00			0.99		
K				0.03		
Na				0.03		
A	1.00			1.00		
Al	9.46			8.49		
Fe^{3+}	1.84			1.89		
Ti^{4+}	0.28			0.82		
Mg	0.26			0.39		
Fe^{2+}				0.33		
Cr^{3+}	0.10			0.01		
Si				0.01		
V^{3+}	0.03					
Mn^{2+}				0.01		
Ca	0.03			0.05		
B	12.00			12.00		

[a] Empirical formula $Ca_{1.03}(Al_{9.46}Fe^{3+}_{1.84}Ti_{0.28}Mg_{0.26}Cr^{3+}_{0.10}V^{3+}_{0.03})_{\Sigma 11.97}O_{19}$. [b] Empirical formula $(Ca_{0.99}K_{0.03}Na_{0.03})_{\Sigma 1.05}(Al_{8.49}Fe^{3+}_{1.89}Ti_{0.82}Mg_{0.39}Fe^{2+}_{0.33}Cr^{3+}_{0.01}Mn^{2+}_{0.01}Si_{0.01})_{\Sigma 11.95}O_{19}$. [c] Calculated on charge balance. Note that n.d. is not detected.

was controlled by the DA^+ acquisition software (Wojdyla et al., 2018). Determination of lattice parameters was carried out using CrysAlis Pro (Rigaku, 2020); data reduction and absorption corrections were processed with XDS (Kabsch, 2010). The crystal structure refinement was performed with Jana2006 (Petříček et al., 2014). Experimental details are summarized in Table S1 of the Supplement. Crystal structures are visualized with VESTA 3 (Momma and Izumi, 2011). Bond valence sums are calculated with BondStr (Rodríguez-Carvajal, 2005) using parameters given by Brown and Altermatt (1985). The original images of the diffraction data show evidence of one-dimensional diffuse scattering. Therefore, selected layers of the reciprocal space

were reconstructed using a modified version of Xcavate (Estermann and Steurer, 1998).

5 Results

5.1 Chemical composition

The studied crystal of kahlenbergite exhibits a homogeneous chemical composition. The results of the electron-microprobe analyses are summarized in Table 1. The kahlenbergite empirical formula, calculated on the basis of 17 oxygen atoms, is $(K_{0.87}Mg_{0.09}Ca_{0.03}Ba_{0.01})_{\Sigma 1}(Al_{9.46}Fe^{3+}_{1.36}Mg_{0.14}Cr^{3+}_{0.02}Si_{0.02})_{\Sigma 11}O_{17}$, and the simplified formula is

$(K,Mg)(Al,Fe^{3+},Mg)_{11}O_{17}$. The ideal formula is $KAl_{11}O_{17}$, which requires 7.75 wt % of K_2O and 92.25 wt % of Al_2O_3. Water and CO_2 were not determined by direct measurements because of the small size of the kahlenbergite crystals and difficulties of selecting pure material. The totals of the microprobe analysis are slightly below 100 wt %. This implies that a small amount of water may be present.

Two varieties of hibonite were found in association with kahlenbergite (Table 2). Their empirical formula was calculated based on 19 oxygen atoms. The majority of the hibonites are low in Ti ($TiO_2 < 5$ wt %) with an average composition of $Ca_{1.03}(Al_{9.46}Fe^{3+}_{1.84}Ti_{0.28}Mg_{0.26}Cr^{3+}_{0.10}V^{3+}_{0.03})_{\Sigma 11.97}O_{19}$, described with the simplified formula as $CaAl_{10}Fe_2O_{19}$. A few of the grains can be considered Ti-rich hibonites ($8.5 < TiO_2 < 9.2$ wt %) with an average composition of $(Ca_{0.99}K_{0.03}Na_{0.03})_{\Sigma 1.05}(Al_{8.49}Fe^{3+}_{1.89}Ti_{0.82}Mg_{0.39}Fe^{2+}_{0.33}Cr^{3+}_{0.01}Mn^{2+}_{0.01}Si_{0.01})_{\Sigma 11.95}O_{19}$ and simplified formula $CaAl_8Fe_2TiMgO_{19}$. The REEs, as often-detected elements in terrestrial hibonites, are below the limit of detection.

The available data on olive subunits show that specific oxygen fugacity during the pyrometamorphic processes within the Hatrurim Complex (Israel) has provided for high-temperature oxygen-bearing minerals that contain mainly Fe^{3+}. However, minerals of the spinel group exceptionally show significant amounts of Fe^{2+}, as reported by Sharygin et al. (2013), Galuskina et al. (2017), Galuskin et al. (2018a), and Vapnik et al. (2007). Therefore, we assume that small amounts of Fe^{2+} may be present in octahedra of the spinel blocks. However, the stoichiometry excludes a significant amount of Fe^{2+} in kahlenbergite and Fe-rich hibonite.

5.2 Raman spectra

The main bands in the Raman spectra of kahlenbergite, $KAl_{11}O_{17}$ (Fig. 5), as well as of hibonite, $CaAl_{10}Fe_2O_{19}$ (Fig. 6), are related to the Al–O vibrations in $(AlO_4)^{5-}$ cm^{-1} (Chukanov et al., 2019; Table 3). The character of the Raman spectra of kahlenbergite and hibonite depends on the crystal orientation (Figs. 5 and 6). The band near 846 cm^{-1} in the hibonite spectra appears only at laser beam polarization along (001) and responds to vibrations in the triangular planar group $(AlO_3)^{3-}$ in the triangular bipyramid (site M2, Fig. 2). In the reflected FTIR spectra of jewellery hibonite, the strong bands of ν_3(Al–O) are at 846 and 785 cm^{-1} (Hainschwang et al., 2010), i.e., at exactly the same positions as in the Raman spectra of the studied hibonite (Fig. 6, Table 3). This way, these bands in the hibonite, as well as in the kahlenbergite, spectra are specified by both symmetric (ν_1) and asymmetric (ν_3) stretching vibrations. The diagnostic bands in the kahlenbergite and hibonite spectra are ones related to K–O vibrations at 180 cm^{-1} and Ca–O at 115 cm^{-1}, respectively (Figs. 5, 6). Interestingly, in the numerous kahlenbergite spectra obtained from (001) faces, we often observed a band at 845 cm^{-1}. We attribute this band
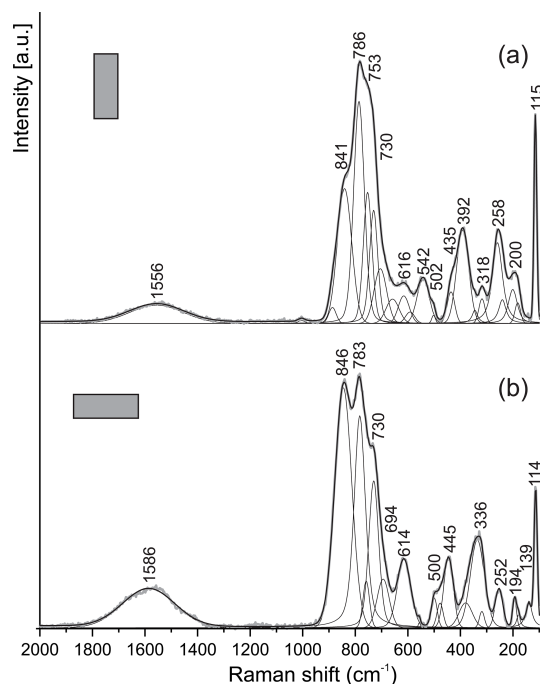
Figure 6. Raman spectra of hibonite for two orientations of crystal. The laser beam is polarized horizontally.

to hibonite inclusions. So in this paper we give only kahlenbergite spectra obtained at the crystal section, which were checked in SEM/EDS and did not contain any inclusions.

5.3 Crystal structure of kahlenbergite

The single-crystal diffraction experiment was carried out using a crystal grain of $30 \times 25 \times 20\,\mu m^3$. Kahlenbergite crystallizes in space group $P6_3/mmc$ (no. 194) with cell parameters $a = 5.6486(1)$ Å, $c = 22.8970(3)$ Å, $V = 632.69(2)$ Å^3 and $Z = 2$. The unit cell dimensions and space group of kahlenbergite correspond to those of synthetic potassium β-alumina; therefore the structure was refined starting from the known structure model (Dernier and Remeika, 1976). The scattering densities on the different positions were determined using the Al atomic scattering factor combined with a refinement of the individual site occupancies.

Compared to synthetic K β-alumina, which often shows considerable amounts of positional and occupational cation disorder, the structure of kahlenbergite is fairly simple (Fig. 7). The final atomic positions and equivalent/isotropic displacement parameters are given in Table 4. Tabulated anisotropic displacement parameters are provided in Table S2 in the Supplement.

The structure of kahlenbergite is made of two S (spinel) and two R (conducting) blocks. Within the R block, the so-called "Beevers–Ross" site at (2/3, 1/3, 1/4) is fully occupied with potassium (Iyi et al., 1989; Peters et al., 1971). The two S blocks are related to each other by a mirror plane

Table 3. Raman bands of kahlenbergite and hibonite (cm^{-1}).

Kahlenbergite		Hibonite		Vibration mode
Spectrum A	Spectrum B	Spectrum A	Spectrum B	
1536	1555	1556	1586	overtone
823	842	841	846	$\nu_3(AlO_4)^{5-}$ or $\nu_1/\nu_3(AlO_3)^{2-}$ in $(AlO_5)^{7-}$
780	784	786	783	$\nu_1/\nu_3(AlO_4)^{5-}$
736	737	730	730	$\nu_1(FeO_4)^{5-}$
682	686		694	$\nu_1(AlO_6)^{9-}$
598	607	616	614	$\nu_1(FeO_6)^{9-}$
546	555	542		$\nu_4(AlO_4)^{5-}$
508	498	502	500	$\nu_4(FeO_4)^{5-}$
439	440	435	445	$\nu(Al-O-Al)$ in $(Al_2O_7)^{8-}$
431	430	392		$\nu(Al-O-Al)$ in $(Al_2O_9)^{12-}$
366	353			
302	306	318	336	$\nu_2(AlO_4)^{5-}$
272	294			
		258	252	$\nu_2(FeO_4)^{5-}$, Ca–O
180	179	200	194	K–O-related vibration
177	176			
		115	139	Ca–O-related vibration
			114	

Note that in the 200–500 cm^{-1} range $\nu(AlO_4)^{5-}$ and $\nu(FeO_4)^{5-}$ vibrations also contribute (Chukanov et al., 2019).

(m[001]) at $z = 1/4$ and $z = 3/4$. The spinel blocks consist of mixed layers with M4 octahedra (Al) and M2 tetrahedra (44 % Fe), sandwiched between two kagome layers with M1 octahedra (8 % Fe) (Fig. 7). The M3 tetrahedra (Al) in the R blocks are connected to the kagome layer by three shared oxygen atoms (O4 site); the remaining corner (O5) interconnects two tetrahedra and is located on the mirror plane. These tetrahedra are the most probable location for the detected minor amount of Si (0.02 apfu). In the final stages of the refinement we located significant residual electron density close to the 3-fold axis ca. 2.58 Å from the potassium site (Fig. 8). Possible explanations are discussed below.

5.4 Crystal structure of Fe^{3+}-rich hibonite

The crystal structure of hibonite with the simplified formula $CaAl_{10}Fe_2O_{19}$ from Mt Parsa (space group $P6_3/mmc$; $Z = 2$; cell parameters $a = 5.6420(2)$ Å, $c = 22.1749(7)$ Å, and $V = 611.31(4)$ Å^3) was refined using the atomic parameters reported by Nagashima et al. (2010) as a starting model.

The Ca position shows minor replacement with K and Na; however, in the refinement the effect was insignificant, and therefore this position is modelled with 100 % Ca. All investigated crystals show cation substitution $Ti^{4+} + (Mg^{2+}, Fe^{2+}) \rightarrow 2Al^{3+}$ which may take place at all five cation positions (M1–M5). In order to unravel the site occupancies, site scattering, bond distances, and bond valence sums have to be considered, and information on cation distribution in magnetoplumbite group minerals and synthetic materials (Holtstam and Hålenius, 2020) has to be taken into account. The final atomic positions, site occupancies, and isotropic displacement parameters are given in Table 5. Tabulated anisotropic displacement parameters are provided in Table S3 in the Supplement. Selected bond lengths are given in Table 6.

As in all hibonite-type structures, the A site is located in the central part of the R block coordinated by 12 oxygen atoms. Bermanec et al. (1996) showed that the average A–O bond distance is virtually independent of the actual species at the A site. This is because of the inflexibility of the R blocks,
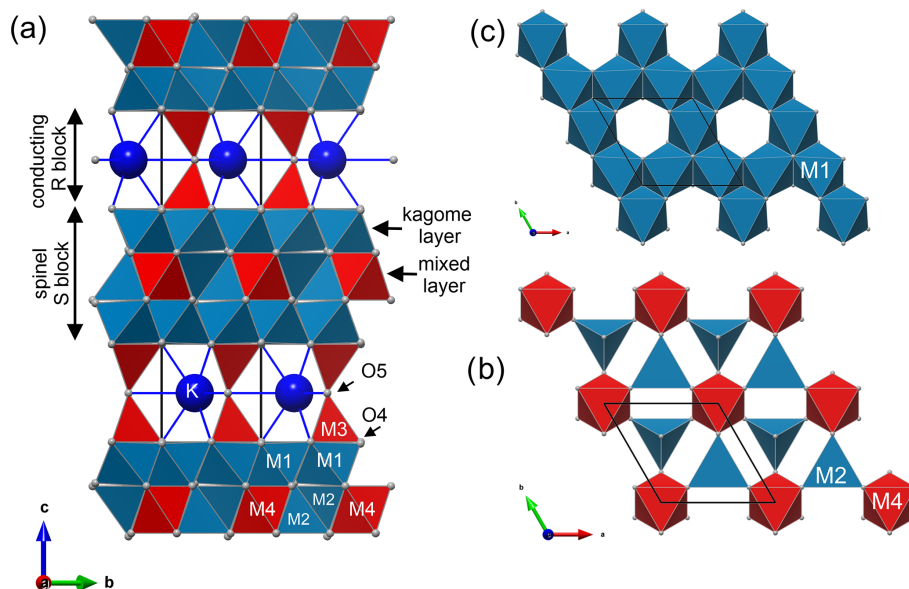
Figure 7. Structure of kahlenbergite. **(a)** Unit cell is made of two spinel (S) blocks and two conducting R blocks. Spinel blocks can be divided along c into mixed layers **(b)** and kagome layers **(c)**. In mixed layers AlO$_6$ octahedra (M4) and (Al$_{0.56}$Fe$_{0.44}$)O$_4$ tetrahedra (M2) share corners. The kagome layer is built by edge-sharing (Al$_{0.92}$Fe$_{0.08}$)O$_6$ octahedra (M1).

Table 4. Kahlenbergite relative atomic coordinates and equivalent/isotropic displacement parameters. The M1 and M2 sites show a mixed Al and Fe occupancy.

Site	Atom type	Occupancy	x	y	z	$U_{(eq)}$
A	K	1	0.6667	0.3333	0.25	0.0236(6)
M1	Al	0.918(8)	0.83212(8)	0.66424(15)	0.10611(4)	0.0062(4)
	Fe	0.082(8)				
M2	Al	0.556(10)	0.3333	0.6667	0.02503(5)	0.0036(4)
	Fe	0.444(10)				
M3	Al	1	0.3333	0.6667	0.17557(7)	0.0048(5)
M4	Al	1	0	0	0	0.0041(5)
O1	O	1	0.1531(2)	0.3062(4)	0.05048(11)	0.0068(7)
O2	O	1	0.50156(18)	0.0031(4)	0.14517(10)	0.0061(7)
O3	O	1	0.6667	0.3333	0.05713(18)	0.0068(9)
O4	O	1	0	0	0.14168(17)	0.0056(8)
O5	O	1	0.3333	0.6667	0.25	0.031(2)

which are actually oxygen close packings with average bond lengths of 2.89–2.91 Å for ferrites and 2.75–2.78 Å for aluminates. As a consequence, small cations like Ca are underbonded. In the structure of Fe^{3+} hibonite, the average Ca–O distance is 2.783 (Table 6) the bond valence sum (BVS) of Ca is 1.33 valence units (v.u.). The very same BVS for Ca atoms is found in CaAl$_{9.47}$Fe$_{2.53}$O$_{19}$ (Medina et al., 2017).

Judged on site-scattering refinements, the two octahedrally coordinated sites (M1 and M5) are considered to be almost fully occupied with aluminium. The octahedral distances at M1 and M5 are slightly larger than in synthetic CaAl$_{12}$O$_{19}$ (Utsunomiya et al., 1988) (0.014 Å and up to 0.03 Å, respectively); furthermore, both sites are underbonded: BVS (M1) is 2.85 and BVS (M5) is 2.72 v.u. Therefore, minor amounts

of Mg can be expected at both sites. The M2 site is a five-coordinated mirror-related split position within the R layer (Figs. 1 and 2). The observed distances are 2.34(3) and 2.085(3) (M2–O1), and 1.791(2) Å (3 × M2–O3). These distances are larger than in the pure AlO$_5$ polyhedra (2.450(4), 2.025(4), 3 × 1.765(3)) of synthetic SrAl$_{12}$O$_{19}$ (Kimura et al., 1990) and smaller than in FeO$_5$ in SrFe$_{12}$O$_{19}$ (2.384(4), 2.157(4), 3 × 1.858(3)) (Kimura et al., 1990). Site occupancy refinement (Al vs. Fe) converged at ca 56 % Fe^{3+} at M2. Site-scattering refinement of the tetrahedrally coordinated M3 site shows ca. 16.9 electrons; therefore occupancy refinement for Al vs. Fe was applied, which resulted in 72 % and 28 %, respectively. The M3–O distances in this tetrahedra (1.8747(18) and 3 × 1.8516(10)) are very

Table 5. Hibonite relative atomic coordinates and equivalent isotropic displacement parameters. The M2, M3, and M4 sites show a mixed occupancy.

Site	Atom type	Occupancy	x	y	z	$U_{(eq)}$
A	Ca	1	0.6667	0.3333	0.25	0.0291(3)
M1	Al	1	0	0	0	0.0083(3)
M2	Al	0.219(3)	0	0	0.7457(15)	0.015(2)
	Fe	0.281(3)	0	0	0.7457(15)	0.015(2)
M3	Al	0.723(4)	0.3333	0.6667	0.02799(3)	0.0070(2)
	Fe	0.277(4)	0.3333	0.6667	0.02799(3)	0.0070(2)
M4	Al	0.641(4)	0.6667	0.3333	−0.18900(2)	0.00724(18)
	Fe	0.219(4)	0.6667	0.3333	−0.18900(2)	0.00724(18)
	Ti	0.14	0.6667	0.3333	−0.18900(2)	0.00724(18)
M5	Al	1	0.16800(3)	0.33599(6)	−0.108282(18)	0.00691(19)
O1	O	1	0	0	0.85119(8)	0.0097(4)
O2	O	1	0.3333	0.6667	−0.05655(8)	0.0091(4)
O3	O	1	−0.18303(15)	0.18303(15)	0.75	0.0156(5)
O4	O	1	0.15234(10)	0.30468(19)	0.05269(5)	0.0101(3)
O5	O	1	0.50478(8)	0.49522(8)	0.35109(5)	0.0100(3)
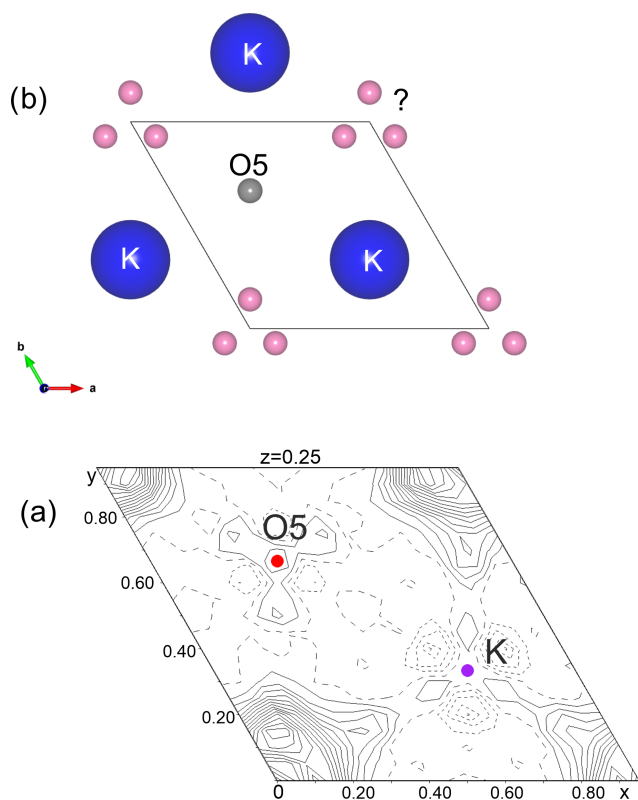
Figure 8. (a) The residual electron density (highest peak 3.1 e− observed on the difference Fourier map in the mirror plane (R block) after refinement and **(b)** possible atom positions.

In our Fe^{3+} hibonite a BVS of ca. 2.37 v.u. (the weighted sum of BVS(Al) = 2.107(3); BVS(Fe^{3+}) = 3.068(5)) indicates significant presence of Mg on the M3 site. According to Holtstam and Hålenius (2020), cations of higher charge (e.g., T^{4+}) prefer the M4 site. As we observe a charge of 17.3 e− at the M4 site, we have fixed the total amount of Ti (as established by EMPA, 0.28 apfu) and refined the remaining density on M4 as Al vs. Fe. With the site population of ∼ 64 % Al, ∼ 22 % Fe, and ∼ 14 % Ti, the total bond valence sum for this site is 2.96 valence units. The chemical composition as obtained from the structure refinement $Ca(Al, Mg)_{10.166} Fe_{1.554} Ti_{0.28} O_{19}$ exhibits more light elements (Al + Mg) than that obtained by the chemical analysis by EMPA.

6 Discussion

6.1 Structural properties of kahlenbergite

In kahlenbergite, the three layers of the S block have pure Al sites, as well as octahedra and tetrahedra with mixed Fe and Al occupancy. In a number of β-alumina compounds, the Al tetrahedra (M2 site) in the central (mixed) spinel blocks is underbonded (Wagner and O'Keeffe, 1988). In synthetic $KAl_{11}O_{17}$ (Iyi et al., 1986) the bond valence sum (BVS) of the M2 site is 2.46 v.u. With increasing iron content, this is the first position to take up iron. In kahlenbergite of the type locality, the M2 site contains 44 % Fe^{3+}, increasing the BVS to 2.49 (weighted sum of BVS(Al) = 2.074(7) and BVS(Fe^{3+}) = 3.020(11)).

Iron at this site has a strong influence on the size and the distortion of the tetrahedra. The pure Al tetrahedra in $KAl_{11}O_{17}$ (Iyi et al., 1989) show an average bond length of 1.799 Å and a volume of 2.991 Å^3, whereas the M2 tetrahe-

close to the ones observed in Myanmar hibonite (Nagashima et al., 2010), where this site contains ∼ 70 % Al, 5 % Zn, and 25 % Mg. Batlle et al. (1991) found that two-valent cations prefer the M3 site in magnetoplumbite structures.

Table 6. Selected bond distances (Å), average bond lengths (Avg.) and bond valence sums (BVSs) up to 3.3 Å in a kahlenbergite structure.

Bond lengths (Å) and BVS* (v.u.) in kahlenbergite		Bond lengths (Å) and BVS (v.u.)* in hibonite	
A = K		A = Ca	
6 × A–O2	2.893(2)	6 × A1–O3	2.8255(7)
6 × A–O5	3.261(2)	6 × A1–O5	2.7437(9)
Avg.	3.016	Avg.	2.783
BVS	0.91	BVS	1.33
M1 = 92 % Al + 8 % Fe		M1 = Al	
2 × M1–O1	2.0260(3)	6 × M1–O4	1.8924(10)
2 × M1–O2	1.848(2)	BVS	2.87
M1–O3	1.969(2)		
M1–O4	1.833(2) × 1	M2 = 44 % Al + 56 % Fe	
Avg.	1.925	M2–O1	2.34(3)
BVS	2.78	M2–O1	2.15(3)
		3 × M2–O3	1.791(2)
		Avg.	1.972(10)
M2 = 56 % Al + 44 % Fe		BVS	2.85
3 × M2–O1	1.857(2)		
M2–O4	1.881(4)	M3 = 72 % Al + 28 % Fe	
Avg.	1.863	M3–O2	1.8747(18)
BVS	2.49	3 × M3–O4	1.8516(10)
		Avg.	1.857
M3 = Al		BVS	2.37
3 × M3–O2	1.787(2)		
M3–O5	1.704(2)	M4 = 64 % Al + 22 % Fe + 14 % Ti	
Avg.	1.766	3 × M4–O3	1.9968(8)
BVS	2.71	3 × M4–O5	1.8967(7)
		Avg.	1.947
M4 = Al		BVS	2.96
6 × M4–O1	1.892(2)		
Avg.	1.892	M5 = Al	
BVS	2.88	M5–O1	1.8716(9)
		M5–O2	1.9816(11)
		2 × M5–O4	1.9967(11)
		2 × M5–O5	1.8355(8)
		Avg.	1.9196(4)
		BVS	2.72
BVS O1	1.80	BVS O1	1.76
BVS O2	1.89	BVS O2	1.69
BVS O3	1.80	BVS O3	1.84
BVS O4	1.75	BVS 04	1.80
BVS O5	1.74	BVS O5	1.80

* Calculated after Brown and Altermatt (1985).

dra in kahlenbergite (with 44 % Fe) exhibit an average bond length of 1.863 Å and a volume of 3.3175 Å^3. These tetrahedra are corner-connected to three pure Al octahedra (M4) in the mixed layer and to the common corner of three M1 octahedra (Al$_{0.92}$Fe$_{0.08}$) in the kagome layer. Due to the low BVS (2.71 v.u.) of M1 in the synthetic KAl$_{11}$O$_{17}$ (Iyi et al., 1986), it is obvious that this site will also be a preferred target for Fe substitution. For comparison, the Fe atoms in KFe$_{11}$O$_{17}$ (Ito et al., 1996) exhibit a more balanced bonding: tetrahedra M2 for example shows a bond distance of 1.9065 Å and a volume of 3.5548 Å^3. Its BVS is 2.69. The influence of the chemical composition on the cell parameters is shown in Table 7.

The unit cell parameters of Fe-free kahlenbergite from Mt Carmel (Griffin et al., 2020a, b), with the almost ideal composition KAl$_{11}$O$_{17}$ (traces of Na, Mg, and Cr), are almost identical to the parameters of pure K β-alumina (Iyi et al., 1989). Kahlenbergite from the type locality (Mt Parsa) with 17 wt % of Fe$_2$O$_3$ shows slightly larger lattice parameters: the increase is ca. 0.9 % and 0.8 % for a and c, respectively.

The presented structure model of kahlenbergite describes an idealized ordered structure. The residual electron density peak (at 0.07, 0.14, 0.25) of 3.1 e− Å^{-3} is located close to the 3-fold axis and may be modelled or explained by one of the following options. Adding/refining atoms (options 1 and 2) further improves the refinement R1 value down to ca. 2.7 %. Without further experimental efforts, the three options cannot be ultimately approved or rejected.

1. If the residual density is explained using an additional K atom, its occupancy refinement will result in ca. 1.4 apfu. This approach is supported by the results of Dernier and Remeika (1976) and Iyi et al. (1986) for synthetic potassium β-alumina. Charge compensation is obtained by nonstoichiometric composition.

2. An alternative explanation is water. To investigate the influence of water on the ion conduction properties, many authors have treated β-alumina compounds with water vapour, air, and liquid water (Marini et al., 1985; McConohy, 2019; Colomban, 2000). Bates et al. (1982) reported the position of water molecules (in hydrated isostructural lithium β-alumina) at approximately the same position as the residual electron density observed in kahlenbergite. Using a water molecule to model the residual density results in 0.76 H$_2$O per formula unit.

3. The residual density is an artefact caused by the observed stacking disorder. As outlined below, hibonite-like R layers or even larger hibonite blocks may be present within kahlenbergite.

Concerning the first option, it has to be noted that the given empirical formula is calculated based on 17 oxygen atoms. If there is excess potassium, as there is in the nonstoichiometric synthetic compounds, there will be more oxygen.

Option 2 is not supported by direct evidence for the presence of water. However, there are indications of water within

Table 7. Cell parameters of selected K β-alumina, K β-ferrite, and selected hibonite-type minerals.

Chem. formula	Mineral name	a (Å)	c (Å)	References
K$_{1.50}$Al$_{11}$O$_{17.25}$		5.598(l)	22.732(5)	Iyi et al. (1986)
KAl$_{11}$O$_{17}$		5.59765(10)	22.7141(4)	Griffin et al. (2020a, b)
KAl$_{9.679}$Fe$_{1.321}$O$_{17}$	kahlenbergite	5.64860(6)	22.8970(3)	this work
KFe$_{11}$O$_{17}$		5.930(4)	23.848(4)	Ito et al. (1996)
CaAl$_{12}$O$_{19}$	hibonite	5.5909(1)	21.9893(4)	Nagashima et al. (2010)
CaFe$_6$Al$_6$O$_{19}$		5.6258	22.084	Harder and Müller-Buschbaum (1977)
CaAl$_{10}$Fe$_2$O$_{19}$	hibonite	5.64325(16)	22.1719(7)	this work
CaAlFe$_{11}^{3+}$O$_{19}$	gorerite	5.8532(4)	22.7730(2)	Galuskin et al. (2019)

kahlenbergite: the total sums of the microprobe analysis are lower than 100 %. Even though kahlenbergite and hibonite are high-temperature minerals, the widespread development of Ca zeolites and hydrosilicates in vesicular spaces of hornfels indicates a late hydrothermal stage, which could have caused partial hydration of kahlenbergite. The other possibility is late hydration during preparation of the thin section. Bates et al. (1982) have investigated hydrated β-alumina compounds using neutron diffraction and IR and Raman spectroscopy and have reported a major absorption band near 3175 cm^{-1}, for symmetric stretching vibrations of the H$_2$O molecule. They have attributed the peaks above 3350 cm^{-1} to OH$^-$ ions, and bands below 2700 cm^{-1} are attributed to H$_3$O$^-$ and H$_5$O$^-$ species. The Raman spectra of kahlenbergite does not exhibit stretching vibration modes for water molecules or any bands below 2700 cm^{-1}, as reported by Bates et al. (1982). It could be argued that a wide symmetric band at 1535 or rather 1555 cm^{-1} in other orientations could be attributed to the bending vibration ν_2 of water molecules normally observed near 1595 cm^{-1}. In the absence of other usually stronger specific water bands, and due to their specific positions, we consider that broad peak at 1535/1555 cm^{-1} to be a first overtone of the strongest band at 780/784 cm^{-1}. Still, cations in β-alumina compounds can be replaced by an H$_3$O$^+$ ion and part of the water can enter into the structure as neutral molecules (Lucazeau, 1983; Colomban, 2000). Therefore, the idea of hydrated kahlenbergite should not be abandoned.

We would like to note that the incorporation of lithium is another option to consider. However, we abandoned this idea for several reasons: in isostructural NaAl$_{11}$O$_{17}$, lithium is located at positions close to the Bevers–Ross site (2/3, 1/3, 1/4) (Edström et al., 1997). Furthermore, pyrometamorphic gehlenite-bearing rocks of the Hatrurim Complex are characterized by low Li contents < 10–20 ppm (Bogoch et al., 1999; our unpublished data) and no Li-bearing minerals have been described in this region. Also, there are no known cases of Li incorporation into the structure of natural hexaferrites and hexaaluminates, which are structurally related to kahlenbergite (Holtstam and Hålenius, 2020).

6.2 Disorder and diffuse scattering

Sections of the reciprocal space of three different crystals (a, b, and c) were reconstructed from raw diffraction data. Figure 9 shows stripes of these sections containing the 00l line. All crystals exhibit one-dimensional diffuse scattering proving that stacking faults of some kind are present. In crystal a additional reflection can be identified (red arrows).

Measuring the peak positions along c^*, it is obvious that a second phase exhibits a 3.3 % smaller lattice parameter c. The length of the c parameter (ca. 22.1 Å) is longer than in the here-observed hibonite CaAl$_{10}$Fe$_2$O$_{19}$ and shorter compared to the synthetic CaFe$_6$Al$_6$O$_{19}$ (Harder and Müller-Buschbaum, 1977) (Table 7). Therefore, we presume that the second phase is Fe-rich hibonite. The structure of kahlenbergite and the Fe^{3+}-rich hibonite contain identical S blocks which are connected by R blocks (Wagner and O'Keeffe, 1988), which is different in the Fe^{3+} analogue of hibonite and kahlenbergite. The R blocks of hibonite contain Ca atoms, AlO$_5$ bipyramids, and further AlO$_6$ octahedra. Therefore, the connecting layers are most likely the source of the disorder. In the investigated kahlenbergite crystals some of the R blocks may be randomly exchanged by hibonite-type R blocks. The extent of this disorder is variable as can be seen in Fig. 9. Crystal b shows the smallest degree of disorder, whereas crystal c exhibits much stronger intensities of the diffuse scattering. Consequently, data of crystal b were used for the structure refinement. Larger and coherently scattering domains of the hibonite-type structure have to be present in crystal a, proven by the occurrence of distinct reflections on a lattice with slightly larger c^* (as discussed above). However, diffuse scattering is present in all investigated single crystals. The presented structure model of kahlenbergite describes an idealized ordered structure.

7 Conclusion – modular structures

Further structures with various stacking of β-alumina, magnetoplumbite, and three-layered spinel blocks are known. Kahn and Thery (1986) reported the structure of the mixed sodium neodymium aluminate Nd$_{0.9}$Na$_{1.29}$Al$_{23}$O$_{36.14}$
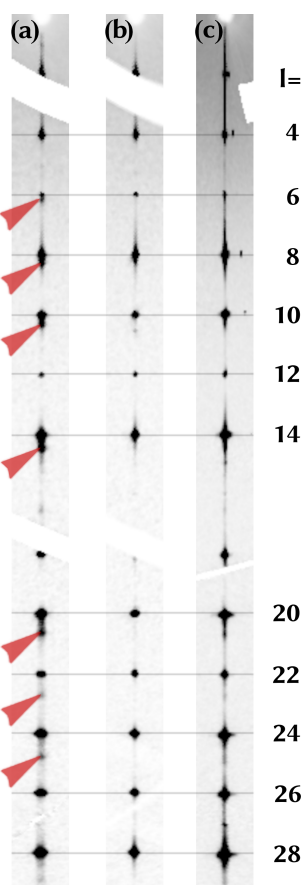
Figure 9. Diffuse scattering of three crystals of kahlenbergite is shown. Stripes (along the 00l line) of the reciprocal space layer 0kl are compared. Crystal **(a)** shows extra reflections (red arrows). which are caused by domains of hibonite, whereas crystal **(c)** exhibits stronger diffuse scattering and only broad maxima at the positions of the hibonite peaks. Data of crystal **(b)** were used for the structure refinement as the crystal's diffuse scattering is weak.

($P\bar{6}m2$; $a = 5.57$ Å; $c = 22.25699$ Å) with "alternate stacking of half β-alumina unit cell and half magnetoplumbite unit cell". The flux-grown compound of Sr$_2$MgAl$_{22}$O$_{36}$ (Iyi and Göbbels, 1996) crystallizes in the same space group ($c = 22.225(5)$) and can be understood as an intermediate structure between SrAl$_{12}$O$_{19}$ (magnetoplumbite structure type; $c = 22.00$ Å) and SrMgAl$_{10}$O$_{17}$ (β-alumina type; $c = 22.399$ Å). This is the first "mixed-layer" structure with only one type of large cation.

The new and unaccredited minerals compositions (Holtstam and Hålenius, 2020) as well as synthesis experiments show that we can expect a lot of new structures of this kind. With three-layered spinel blocks and the magnetoplumbite type of structure in the Hatrurim Complex, the following are found: barioferrite BaFe$_{12}^{3+}$O$_{19}$ (Krzątała et al., 2018; Murashko et al., 2011) and gorerite (CaAlFe$_{11}$O$_{19}$) (Galuskin et al., 2019) as well as the Fe^{3+} analogue of kahlenbergite KFe$_{11}$O$_{17}$ (IMA2020-

091; Galuskin et al., 2021). The first natural hexaferrite with mixed β-alumina and magnetoplumbite structure, KBaMg$_4$Fe$_{31}$O$_{52}$, was found in Jabel Harmun, the Hatrurim Complex (Galuskin et al., 2018b). This structure exhibits an ordered arrangement of a half β-alumina type of cell of KMg$_2$Fe$_{15}$O$_{25}$ and half magnetoplumbite cell of BaMg$_2$Fe$_{16}$O$_{27}$, with five-layered spinel blocks.

Author contributions. EG, IG, and YV conducted fieldwork, microprobe analysis, and Raman spectroscopy; identified optical properties; and interpreted the results. HK performed experiments at the synchrotron and analysed diffuse scattering. BK performed experiments at the synchrotron and analysed the crystal structure, interpreted the results, and wrote the paper, with help from all co-authors.

References

Al-Shantir, O., Keppert, M., Vrabec, M., and Trník, A.: Influence of compression pressure on thermal expansion, bulk density, and porosity of electroporcelain after firing, AIP Conference Proceedings 2275, 020001, https://doi.org/10.1063/5.0025878, 2020.

Ballhaus, C., Helmy, H. M., Fonseca, R. O. C., Wirth, R., Schreiber, A., and Jöns, N. Ultra-reduced phases in ophiolites cannot come

from Earth's mantle, Am. Mineral., https://doi.org/10.2138/am-2021-7612, in press, 2021.

Bates, J. B., Dudney, N. J., Brown, G. M., Wang, J. C., and Frech, R.: Structure and spectra of H$_2$O in hydrated β-alumina, J. Chem. Phys., 77, 4838–4856, https://doi.org/10.1063/1.443725, 1982.

Batlle, X., Obradors, X., Rodríguez-Carvajal, J., Pernet, M., Cabañas, M. V., Vallet, M.: Cation distribution and intrinsic magnetic properties of Co-Ti–doped M–type barium ferrite, J. Appl. Phys., 70, 1614–1623, https://doi.org/10.1063/1.349526, 1991.

Bentor, Y. K.: Israel, in: Lexique Stratigraphique International, Asie, vol. III (10.2), p. 80, 1960.

Bentor, Y. K. and Vroman, A.: The geological map of Israel, 1 : 100,000, Ser. A. – the Negev, Sheet 16: Mount Sdom, explanatory text, Isr. Geol. Survey, 117, 1960.

Bermanec, V., Holtstam, D., Sturman, D., Criddle, A., Back, M., and Scavnicar, S.: Nežilovite, a new member of the magnetoplumbite group, and the crystal chemistry of magnetoplumbite and Hibonite, Can. Miner., 34, 1287–1297, 1996.

Bogoch, R., Gilat, A., Yoffe, O., and Ehrlich, S.: Rare earth and trace element distributions in the Mottled Zone complex, Israel, Israel J. Earth Sci., 48, 225–234, 1999.

Brown, I. D. and Altermatt, D.: Bond-valence parameters obtained from a systematic analysis of the Inorganic Crystal Structure Database, Acta Crystallogr. B, 41, 244–247, https://doi.org/10.1107/S0108768185002063, 1985.

Chukanov, N. V., Vorobei, S. S., Ermolaeva, V. N., Varlamov, D. A., Plechov, P. Y., and Jan, S.: New Data on Chemical Composition and Vibrational Spectra of Magnetoplumbite-Group Minerals, Geol. Ore Depos., 61, 637–646, 2019.

Collin, G., Boilot, J. P., and Comes, R.: Host lattices and superionic properties in β- and β''-alumina. II. Homogeneity ranges and conductivities, Phys. Rev. B, 34, 5850–5861, https://doi.org/10.1103/PhysRevB.34.5850, 1986a.

Collin, G., Boilot, J. P., Colomban, Ph., and Comes, R.: Host lattices and superionic properties in β- and β''-alumina. I. Structures and local correlations, Phys. Rev. B, 34, 5838–5849, https://doi.org/10.1103/PhysRevB.34.5838, 1986b.

Colomban, P.: Vibrational study of hydrogen beta alumina, J. Phys. C Solid State Phys., 14, 4325, https://doi.org/10.1088/0022-3719/14/29/020, 2000.

Dernier, P. D. and Remeika, J. P.: Structural determinations of single-crystal K β-alumina and cobalt-doped K β-alumina, J. Solid State Chem. Fr., 17, 245–253, https://doi.org/10.1016/0022-4596(76)90129-8, 1976.

Edström, K., Gustafsson, T., Thomas, J. O., and Farrington, G. C.: Li+/Na+ β-alumina: A combined single-crystal neutron and X-ray diffraction study, Acta Crystallographica B, 53, 631–638, https://doi.org/10.1107/S0108768197099606, 1997.

Estermann, M. A. and Steurer, W.: Diffuse scattering data acquisition techniques, Phase Transit., 67, 165–195, https://doi.org/10.1080/01411599808219193, 1998.

Galuskin, E., Krüger, B., Galuskina, I., Krüger, H., Vapnik, Y., Wojdyla, J., and Murashko, M.: New Mineral with Modular Structure Derived from Hatrurite from the Pyrometamorphic Rocks of the Hatrurim Complex: Ariegilatite, BaCa$_{12}$(SiO$_4$)$_4$(PO$_4$)$_2$F$_2$O, from Negev Desert, Israel, Minerals, 8, 109, https://doi.org/10.3390/min8030109, 2018a.

Galuskin, E. V., Galuskina, I. O., Widmer, R., and Armbruster, T.: First natural hexaferrite with mixed β-ferrite (β-alumina) and magnetoplumbite structure from Jabel Harmun, Palestinian Autonomy, Eur. J. Mineral., 30, 559–567, https://doi.org/10.1127/ejm/2018/0030-2697, 2018b.

Galuskin, E. V., Krüger, B., Galuskina, I. O., Krüger, H., Vapnik, Y., Pauluhn, A., and Olieric, V.: Levantite, KCa$_3$(Al$_2$Si$_3$)O$_{11}$(PO$_4$), a new latiumite-group mineral from the pyrometamorphic rocks of the Hatrurim Basin, Negev Desert, Israel, Mineral. Mag., 83, 713–721, https://doi.org/10.1180/mgm.2019.37, 2019.

Galuskin, E. V., Krüger, H., Galuskina, I. O., Krüger, B., Nejbert, K., and Vapnik, Y.: Shagamite, IMA 2020-091, CNMNC Newsletter 60, Miner. Mag., 85, https://doi.org/10.1180/mgm.2021.30, 2021.

Galuskina, I. O., Galuskin, E. V., Pakhomova, A. S., Widmer, R., Armbruster, T., Krüger, B., Grew, E. S., Vapnik, Y., Dzierażanowski, P., and Murashko, M.: Khesinite, Ca$_4$Mg$_2$Fe$^{3+}_{10}$O$_4$[(Fe$^{3+}_{10}$Si$_2$)O$_{36}$], a new rhönite-group (sapphirine supergroup) mineral from the Negev Desert, Israel – natural analogue of the SFCA phase, Eur. J. Mineral., 101–116, https://doi.org/10.1127/ejm/2017/0029-2589, 2017.

Geller, Y. I., Burg, A., Halicz, L., and Kolodny, Y.: System closure during the combustion metamorphic "Mottled Zone" event, Israel, Chem. Geol., 334, 25–36, https://doi.org/10.1016/j.chemgeo.2012.09.029, 2012.

Griffin, W. L., Gain, S. E. M., Saunders, M., Cámara, F., Bindi, L., Spartà, D., Toledo, V., and O'Reilly, S. Y.: Cr$_2$O$_3$ in Corundum: Ultra-high contents under reducing conditions, Am. Mineral., in press, 2020a.

Griffin, W. L., Gain, S. E. M., Cámara, F., Bindi, L., Shaw, J., Alard, O., Saunders, M., Huang, J.-X., Toledo, V., and O'Reilly, S. Y.: Extreme reduction: Mantle-derived oxide xenoliths from a hydrogen-rich environment, Lithos, 358–359, 105404, https://doi.org/10.1016/j.lithos.2020.105404, 2020b.

Gross, S.: The mineralogy of the the the Hatrurim Formation, Israel, Geological Survey of Israel, 70, 1–80, 1977.

Hainschwang, T., Notari, F., Massi, L., Armbruster, T., Rondeau, B., Fritsch, E., and Nagashima, M.: Hibonite: A new Gem mineral from Myanmar, GEMS Gemology, 46, 135–138, https://doi.org/10.5741/GEMS.46.2.135, 2010.

Harder, M. and Müller-Buschbaum, H.: Notizen: CaFe$_6$Al$_6$O$_{19}$ mit Magnetoplumbit Struktur / CaFe$_6$Al$_6$O$_{19}$ with magnetoplumbite structure, Z. Naturforschung B, 32, 833–834, https://doi.org/10.1515/znb-1977-0723, 1977.

Holtstam, D. and Hålenius, U.: Nomenclature of the magnetoplumbite group, Mineral. Mag., 84, 376–380, https://doi.org/10.1180/mgm.2020.20, 2020.

Ito, S., Kurosawa, H., Akashi, K., Michiue, Y., and Watanabe, M.: Crystal structure and electric conductivity of K$^+$-β-ferrite with ideal composition KFe$_{11}$O$_{17}$, Solid State Ion., 86–88, 745–750, https://doi.org/10.1016/0167-2738(96)00164-6, 1996.

Iyi, N. and Göbbels, M.: Crystal structure of the new magnetoplumbite-related compound in the system SrO–Al$_2$O$_3$–MgO, J. Solid State Chem., 122, 46–52, https://doi.org/10.1006/jssc.1996.0080, 1996.

Iyi, N., Inoue, Z., and Kimura, S.: The crystal structure and cation distribution of highly nonstoichiometric magnesium-doped potassium β-alumina, J. Solid State Chem., 61, 236–244, https://doi.org/10.1016/0022-4596(86)90027-7, 1986.

Iyi, N., Takekawa, S., and Kimura, S.: Crystal chemistry of hexaaluminates: β-alumina and magnetoplumbite structures, J. Solid State Chem., 83, 8–19, https://doi.org/10.1016/0022-4596(89)90048-0, 1989.

Kabsch, W.: XDS, Acta Crystallogr. D Biol. Crystallogr., 66(2), 125–132, https://doi.org/10.1107/S0907444909047337, 2010.

Kahn, A. and Thery, J.: Structure of a sodium-neodymium aluminate with mixed β-alumina and magnetoplumbite structure – ScienceDirect, J. Solid State Chem., 64, 102–107, https://doi.org/10.1016/0022-4596(86)90126-X, 1986.

Kim, D.-G., Moosavi-Khoonsari, E., and Jung, I.-H.: Thermodynamic modeling of the K$_2$O-Al$_2$O$_3$ and K$_2$O-MgO-Al$_2$O$_3$ systems with emphasis on β- and β''-aluminas, J. Eur. Ceram. Soc., 38, 3188–3200, https://doi.org/10.1016/j.jeurceramsoc.2018.02.030, 2018.

Kimura, K., Ohgaki, M., Tanaka, K., Morikawa, H., and Marumo, F.: Study of the bipyramidal site in magnetoplumbite-like compounds, SrM$_{12}$O$_{19}$ (M = Al, Fe, Ga), J. Solid State Chem., 87, 186–194, https://doi.org/10.1016/0022-4596(90)90081-8, 1990.

Kohn, J. A. and Eckart, D. W.: Stacking relations in the hexagonal ferrites and a new series of mixed-layer structures, Z. Krist.-Cryst. Mater., 119, 454–464, https://doi.org/10.1524/zkri.1964.119.5-6.454, 1964.

Krüger, B., Galuskin, E. V., Galuskina, I.O., Krüger, H. and Vapnik, Y. (2019) Kahlenbergite, IMA 2018-158, CN-MNC Newsletter No. 49: Mineralogical Magazine, 83, https://doi.org/10.1180/mgm.2019.35, 2019.

Krzątała, A., Panikorovskii, T. L., Galuskina, I. O., and Galuskin, E. V.: Dynamic Disorder of Fe^{3+} Ions in the Crystal Structure of Natural Barioferrite, Minerals, 8, 340, https://doi.org/10.3390/min8080340, 2018.

Litasov, K. D., Kagi, H., and Bekker, T. B.: Enigmatic super-reduced phases in corundum from natural rocks: possible contamination from artificial abrasive materials or metallurgical slags, Lithos, 340–341, 181–190, 2019.

Lucazeau, G.: Infrared, Raman and neutron scattering studies of β- and β''-alumina: a static and dynamical structure analysis, Solid State Ion., 8, 1–25, https://doi.org/10.1016/0167-2738(83)90035-8, 1983.

Marini, A., Flor, G., Massarotti, V., McGhie, A. R., and Farrington, G. C.: Hydration and carbonation of beta alumina powders, J. Electrochem. Soc., 132, 1250, https://doi.org/10.1149/1.2114082, 1985.

McConohy, G.: The ionic resistance and chemical stability of polycrystalline K-β'' alumina in aqueous solutions at room temperature, Solid State Ion., 337, 82–90, 2019.

Medina, E. A., Li, J., and Subramanian, M. A.: Colored oxides with hibonite structure II: Structural and optical properties of CaAl$_{12}$O$_{19}$-type pigments with chromophores based on Fe, Mn, Cr and Cu, Prog. Solid State Chem. Res., 45–46, 9–29, https://doi.org/10.1016/j.progsolidstchem.2017.02.002, 2017.

Momma, K. and Izumi, F.: VESTA 3 for three-dimensional visualization of crystal, volumetric and morphology data, J. Appl. Crystallogr., 44, 1272–1276, https://doi.org/10.1107/S0021889811038970, 2011.

Murashko, M. N., Chukanov, N. V., Mukhanova, A. A., Vapnik, E., Britvin, S. N., Polekhovsky, Yu. S., and Ivakin, Yu. D.: Barioferrite BaFe12O19: A new mineral species of the magnetoplumbite group from the Haturim Formation in Israel, Geol. Ore De-pos., 53, 558–563, https://doi.org/10.1134/S1075701511070142, 2011.

Nagashima, M., Armbruster, T., and Hainschwang, T.: A temperature-dependent structure study of gem-quality hibonite from Myanmar, Mineral. Mag., 74, 871–885, https://doi.org/10.1180/minmag.2010.074.5.871, 2010.

Novikov, I., Vapnik, Y., and Safonova, I.: Mud volcano origin of the Mottled Zone, South Levant, Geosci. Front., 4, 597–619, https://doi.org/10.1016/j.gsf.2013.02.005, 2013.

Pawlowski, L. and Blanchart, P.: Industrial Chemistry of Oxides for Emerging Ap, Wiley-Blackwell, Hoboken, NJ, 2018.

Peters, C. R., Bettman, M., Moore, J. W., and Glick, M. D.: Refinement of the structure of sodium β-alumina, Acta Crystallogr. Sect. B, 27, 1826–1834, https://doi.org/10.1107/S0567740871004862, 1971.

Petříček, V., Dušek, M., and Palatinus, L.: Crystallographic Computing System JANA2006: General features, Z. Krist.-Cryst. Mater., 229, 345–352, https://doi.org/10.1515/zkri-2014-1737, 2014.

Rigaku: CrysAlisProSoftware System, Version 171.40.53, Rigaku Oxford Diffraction Ltd, Yarnton, Oxfordshire, England, 2020.

Rodríguez-Carvajal, J.: The program BondStr and its GUI GBond-Str, available at: http://mill2.chem.ucl.ac.uk/ccp/web-mirrors/plotr/BondStr/Bond_Str.htm (last access: 1 July 2021), 2005.

Sharygin, V. V.: A hibonite-spinel-corundum-hematite assemblage in plagioclase-clinopyroxene pyrometamorphic rocks, Hatrurim Basin, Israel: mineral chemistry, genesis and formation temperatures, Mineral. Mag., 83, 123–135, https://doi.org/10.1180/mgm.2018.138, 2019.

Sharygin, V. V., Lazic, B., Armbruster, T. M., Murashko, M. N., Wirth, R., Galuskina, I. O., Galuskin, E. V., Vapnik, Y., Britvin, S. N., and Logvinova, A. M.: Shulamitite Ca$_3$TiFe^{3+}AlO$_8$ – a new perovskite-related mineral from Hatrurim Basin, Israel, Eur. J. Mineral., 97–111, https://doi.org/10.1127/0935-1221/2013/0025-2259, 2013.

Shen, S., Chen, L., Li, A., Dong, T., Huang, Q., and Xu, W.: Diaoyudaoite – a new mineral, Acta Mineral. Sin., 6, 224–227, 1986.

Sorokina, E. S. and Iospa, A. V.: Slags as a new type of mineral resource: special features of technogenic ruby and diaoyudaoite of wastes from Cr-V production, European Mineralogical Conference, Vol. 1, EMC2012-733, 2012.

Utsunomiya, A., Tanaka, K., Morikawa, H., Marumo, F., and Kojima, H.: Structure refinement of CaO·6Al$_2$O$_3$, J. Solid State Chem., 75, 197–200, https://doi.org/10.1016/0022-4596(88)90317-9, 1988.

Vapnik, Y., Sharygin, V. V., Sokol, E. V., and Shagam, R.: Paralavas in a combustion metamorphic complex: Hatrurim Basin, Israel, in: Geology of Coal Fires: Case Studies from Around the World, Geological Society of America, 18, 1–21, 2007.

Wagner, T. R. and O'Keeffe, M.: Bond lengths and valences in aluminates with the magnetoplumbite and β-alumina structures, J. Solid State Chem., 73, 211–216, https://doi.org/10.1016/0022-4596(88)90071-0, 1988.

Wojdyla, J. A., Kaminski, J. W., Panepucci, E., Ebner, S., Wang, X., Gabadinho, J., and Wang, M.: DA+ data acquisition and analysis software at the Swiss Light Source macromolecular crystallography beamlines, J. Synchrotron Radiat., 25, 293–303, https://doi.org/10.1107/S1600577517014503, 2018.

Ying, Y., Zhongyue, S., Shimizu, M., and Shimazaki, H.: Comparison between metallurgical byproduct beta-NaAl$_{11}$O$_{17}$ and diaoyudaoite and discussion on the possible source of diaoyudaoite, Kuangwu Xuebao, 18, 97–100, 1998 (in Chinese).

Zhu, N., Guo, F., Li, Y., Shen, S., Chen, L., and Li, A.: Study on crystal structure of diaoyudaoite, Huaxue Xuebao, 50, 527–532, 1992 (in Chinese).